International Journal of
Network Dynamics and Intelligence (IJNDI)

Article

Dynamic-Coding-Based SMC with Multi-Node Protocol under Gilbert-Elliott Channel: An Intelligent Bit-Rate Pre-Allocation Method

Pengcheng Zhang, Zhiru Cao *, and Chen Peng *

Shanghai Key Laboratory of Power Station Automation Technology, School of Mechatronic Engineering and Automation, Shanghai University, Shanghai 200444, China
* Correspondence: zhiru_cao@shu.edu.cn (Z.C.); c.peng@shu.edu.cn (C.P.)
Received: 2 April 2026; Revised: 3 June 2026; Accepted: 25 July 2026; Published: 17 August 2026

Abstract: This paper is concerned with a dynamic-coding-based sliding mode control and intelligent bit-rate pre-allocation method for networked control systems under Gilbert-Elliott channels. To alleviate limited communication bandwidth and packet-length-dependent packet dropout, a channel-guided multi-node round-robin-like protocol is proposed. This protocol allows the sensor side to utilize previous channel mode information to dynamically determine the number of accessing nodes, thereby effectively preventing a surge in packet dropout probability when network conditions deteriorate. Furthermore, a dynamic quantization encoding-decoding mechanism is designed to encapsulate channel modes, zoomed state to be quantized, and dynamic quantization parameters into a binary packet, while an input-holding strategy at the receiver precisely compensates for potential state losses. Crucially, to maximize steady-state control precision, the minimization of the convergent upper bound is transformed into a mixed-integer programming problem. An intelligent optimization scheme combining the simulated annealing algorithm with linear matrix inequalities is proposed to optimally allocate bit rates among different nodes subject to total bandwidth constraints. Theoretical analysis proves that the closed-loop system achieves exponential ultimate boundedness in mean square and ensures the reachability of the sliding domain. Finally, simulation results verify the effectiveness of the proposed strategy.

Keywords: Gilbert-Elliott channels; multi-node protocol; dynamic encoding-decoding scheme; sliding mode control; bit-rate allocation

1. Introduction

In recent years, networked control systems (NCSs) have garnered extensive attention and application in fields such as industrial automation [1, 2], energy systems [3, 4], and unmanned systems [5, 6] due to their significant advantages, including resource sharing, low maintenance costs, and high scalability. The integration of communication networks into closed-loop control systems inevitably breaks the ideal assumption of traditional point-to-point transmission. Network uncertainties, such as limited channel bandwidth, network-induced delays, and packet dropout, often severely degrade control performance and may even lead to system instability [7–10].

To alleviate the congestion pressure caused by limited communication bandwidth, implementing communication scheduling protocols or event-triggered mechanisms between sensors and controllers to regulate data transmission has become an effective solution. The round-robin protocol (RRP), weighted try-once-discard protocol (WTODP), and stochastic communication protocol (SCP) have been widely applied in state estimation of complex stochastic networks, security control of nonlinear systems, and finite-horizon filtering for time-varying systems [11–15]. Nevertheless, conventional single-node protocols permit only a single node to access the network at each sampling instant, which not only neglects the dynamic impact of network status but also results in the loss of critical state data from unselected nodes.

To overcome the limitations of single-node scheduling, multi-node communication protocols have been proposed. Multi-node protocols allow multiple sensor nodes to be encapsulated into a single data packet for simultaneous transmission, significantly increasing data throughput under bandwidth constraints while enhancing system adaptability and data fault tolerance. For different scenarios, multi-node SCP has been applied to sliding mode control (SMC) of fuzzy switched systems [16] and secure filtering of multi-rate nonlinear systems [17], while multi-node RRP has been adopted for H_∞ control of singularly perturbed systems [18]. The aforementioned studies have demonstrated from different dimensions the significant advantages of multi-node parallel transmission in mitigating communication bottlenecks and enhancing system performance.

In practical communication networks, packet dropout is an unavoidable phenomenon. To accurately describe this uncertainty, early studies typically employed Bernoulli independent and identically distributed models to characterize the random dropout process or used standard Markov jump models to describe network status evolution. For stochastic Markov jump systems (MJSs), Bernoulli random variables have been used to model dropouts with imprecise occurrence probabilities [19], while a Markov packet dropout model has been introduced to capture temporal interdependencies in connected vehicle platoons [20]. It should be pointed out that real-world complex network environments often exhibit bursty and state-dependent congestion characteristics. For instance, the packet arrival probability under favorable network conditions is much higher than that under adverse conditions. Fixed dropout probability models struggle to capture such dynamic variations. Consequently, the Gilbert-Elliott (G-E) channel model has been introduced into control system design [21]. The G-E model employs a two-mode time-homogeneous Markov chain to precisely partition the communication channel into good and bad modes, which provides a more accurate description of the dynamic switching mechanism between network status and the resulting fluctuations in communication quality. Since the pioneering G-E model was proposed in [22] for burst-noise channels, it has been widely applied to characterize time-correlated packet dropout, supporting modeling and co-design research in areas such as SMC for NCSs [23] and non-fragile H_∞ filtering for multi-rate time-delayed systems [24].

Beyond communication scheduling protocols, quantization and encoding-decoding techniques are core methods for alleviating bandwidth constraints. In digital network communication, mapping continuous system states into finite discrete values and performing binary encoding is a prerequisite for signal transmission. Although early studies have achieved classic results in system stabilization, coarsest quantization design, and super-twisting SMC using static uniform and logarithmic quantizers [25–27], the fixed quantization parameters in these studies face limitations in balancing a wide range with high precision. To overcome these deficiencies, dynamic quantization has emerged as a research hotspot. By adjusting parameters online, dynamic quantizers adaptively scale the quantization range based on system state magnitudes. Dynamic quantization parameters are divided into time-dependent and state-dependent types. Time-dependent parameters decrease monotonically and are prone to saturation under perturbations. In contrast, state-dependent parameters eliminate this risk but necessitate transmission across the network for decoding. To overcome the limitations of static quantization, dynamic strategies have been developed. Under limited coding length, an adaptive adjustment strategy has been proposed in [28] to clarify the direct impact of coding length on the SMC convergence bound. For hidden MJSs under constrained bit rates, a state-dependent adaptive quantization scheme has been designed in [29] to achieve exponential ultimate boundedness (EUB). More recently, a dynamic coding and time-varying packet length optimization method has been introduced to improve bandwidth utilization and reduce quantization errors in lossy digital networks [30].

In addressing complex systems with parameter perturbations and external disturbances, SMC is considered one of the most promising robust control strategies due to its complete invariance to matched uncertainties and excellent transient response performance [31–33]. With the proliferation of NCSs, designing effective sliding mode controllers under communication scheduling protocols has attracted widespread academic attention. For SMC under multi-node protocols, adaptive dynamic output-feedback SMC has been developed in [34] to cope with node selection fluctuations during system switching. Meanwhile, a token-dependent SMC strategy has been proposed in [35] to achieve consensus for nonlinear multi-agent systems under resource constraints. Furthermore, to maintain SMC robustness under limited bandwidth, the integration of dynamic encoding-decoding mechanisms with SMC has been explored for the joint design of bit-rate allocation and control performance. A multi-communication-scene-aware sliding mode controller for high-rate G-E networks has been established in [36] by integrating a hybrid scheduling mechanism with adaptive dynamic coding, effectively reducing quantization errors and enhancing robustness.

Notably, when addressing the complex joint design of network resource allocation and controller parameters, control theory often encounters highly nonlinear constraints or mixed-integer programming problems. Consequently, leveraging modern optimization algorithms for parameter searching has become a vital trend to overcome the academic bottlenecks of analytical methods [37]. Modern optimization algorithms have been increasingly leveraged to handle complex co-design problems. A genetic algorithm (GA) has been used to optimize dynamic event-triggered mechanisms in MJSs [38], and particle swarm optimization with adaptive weights has been applied to steering control of unmanned vehicles [39]. Among various heuristic approaches, simulated annealing algorithm (SAA) stands out as a stochastic optimization method based on a Monte-Carlo iterative strategy, possessing a strong ability to escape local optima. In dealing with discrete combinatorial optimization and mixed-integer programming problems, SAA has demonstrated significant superiority and efficiency. For instance, SAA has been employed in [40] to globally optimize SMC parameters for reentry vehicles, demonstrating superior robustness over GA. In [41], SAA has been integrated into event-triggered mechanisms to balance control performance and resource consumption in nonlinear MJSs.

Despite the rich research outcomes in these respective branches, the deep integration of multi-node scheduling, dynamic quantization encoding-decoding, and SMC strategies within the G-E channel environment remains an urgent theoretical challenge. Particularly when the total bit rate that encapsulates channel modes, quantized states, and dynamic parameters is limited, few studies have provided a systematic solution for intelligently pre-allocating bit rates to minimize quantization errors and maximize steady-state control precision.

Motivated by these challenges, this paper investigates a dynamic-coding-based SMC and intelligent bit-rate pre-allocation method under G-E channels. The main contributions are summarized in the following three aspects:

(1) A protocol-channel dependency relationship is established by mapping the G-E channel modes to the node-accessing strategy, which allows the proposed multi-node protocol to adaptively scale the number of active nodes according to real-time network conditions. Under such a multi-node protocol, the communication load remains compatible with the time-varying network capacity.

(2) A mode-led dynamic encoding mechanism is established. Since the proposed multi-node protocol relies on the G-E channel mode, it is necessary to transmit the mode information across the network. Accordingly, a dynamic encoding mechanism is designed to encapsulate the current channel mode into the transmitted data packet to ensure real-time update of transmission node count based on the obtained channel mode.

(3) An intelligent bit-rate optimization scheme based on the intersection of SAA and linear matrix inequalities (LMIs) is proposed. The minimization of the convergent upper bound (CUB) is transformed into a mixed-integer programming problem subject to total bandwidth and LMI constraints. Using SAA, optimal bit-rate allocation among different nodes is achieved, significantly enhancing the steady-state control precision of the system.

2. Problem Formulation

To construct a rigorous theoretical analysis framework, this section will sequentially establish a system model, describe channel characteristics, and introduce the proposed communication protocol and encoding-decoding strategy.

2.1. System Model

Consider the NCS as

$$x(k+1) = \big(A + \tilde{A}(k)\big)x(k) + B(u(k) + f(k)), \tag{1}$$

where A and B are constant matrices with B having full column rank; $x(k) \in \mathbb{R}^n$ and $u(k) \in \mathbb{R}^m$ are the state and the control input, respectively. Moreover, $\tilde{A}(k)$ is the norm-bounded parameter uncertainty with $\tilde{A}(k) \triangleq EL(k)H$, and the unknown time-varying matrix $L(k)$ satisfies $L^{\top}(k)L(k) \leq I$. The unknown external perturbation $f(k)$ satisfies $\|f(k)\| \leq \bar{f}$ with $\bar{f}$ being a known constant, and E, H are known matrices.

In the control system illustrated in Figure 1, the signal transmission process is as follows. Sensors collect the system state $x(k)$ in real time, and then a multi-node round-robin-like protocol (MN-RRLP) selects a subset of nodes and packs their states $\{x_j(k)\}$ into a data packet. This packet undergoes dynamic quantization and encoding by an encoder, and is transmitted over a G-E channel. The sender of the network adaptively adjusts the transmission strategy according to the previous channel mode, i.e., good or bad mode. At the receiving end, the decoder decodes the received binary data to recover information such as channel mode $\hat{\theta}(k)$, quantized states $\{\vec{x}_j(k)\}$, and quantization parameter, and compensates for any lost states using historical data stored in a buffer. Based on the decoded state $\hat{x}(k)$, the controller generates a control signal $u(k)$, which is finally applied to the plant via an actuator, thereby closing the control loop.

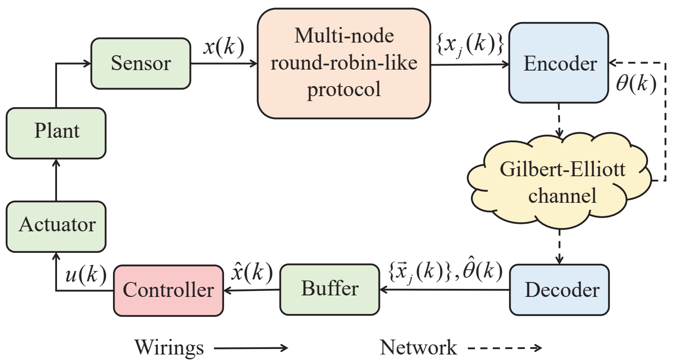

Figure 1. The block diagram of the considered control system.

2.2. G-E Channel

In practical communication networks, due to the complex and time-varying network environment, the probability of packet arrival may not always be fixed, i.e., the channel mode may be random. Generally speaking, the probability of packet arrival under good network conditions is much higher than that under bad conditions, meaning that the probability of packet arrival varies depending on the network condition. Thus, the G-E model is utilized to describe the communication channel mode as a two-mode time-homogeneous Markov chain, and a binary stochastic variable $\theta(k) \in \{-1, 1\}$ is used to indicate whether the channel is in a bad or good mode at this instant. When the channel is in the good mode, i.e., $\theta(k) = 1$, the packet is successfully received. Accordingly, when the channel is in the bad mode, i.e., $\theta(k) = -1$, packet dropout may occur.

The transition probability of the Markov chain $\{\theta(k)\}$ describing the transition between the two modes is

$$g_{t,v} \triangleq \Pr\{\theta(k) = v \mid \theta(k-1) = t\}, \quad t, v \in \{-1, 1\} \tag{2}$$

with $g_{t,v} \in [0, 1]$ and $g_{t,-1} + g_{t,1} = 1$. Correspondingly, the transition probability matrix is expressed as

$$G \triangleq [g_{t,v}]_{2\times 2} \triangleq \begin{bmatrix} g_{-1,-1} & g_{-1,1} \\ g_{1,-1} & g_{1,1} \end{bmatrix} = \begin{bmatrix} 1-b & b \\ a & 1-a \end{bmatrix}, \tag{3}$$

where b refers to the probability of channel environment transferring from bad mode to good mode, and a represents the probability of channel environment transferring from good mode to bad mode. Accordingly, the probabilities of the channel environment being in the bad and good modes are, respectively, $\bar{\omega}_1 = \frac{a}{a+b}$ and $\bar{\omega}_2 = \frac{b}{a+b}$ in the statistical sense.

The random variable $\pi_1(k) \in \{0, 1\}$, which satisfies the Bernoulli distribution, indicates whether a single-node-length packet dropout occurs when the channel is in the bad mode. When the channel is in the bad mode, $\pi_1(k) = 1$ indicates that no packet dropout occurs, while $\pi_1(k) = 0$ means the occurrence of packet dropout. The Bernoulli distribution sequence $\{\pi_1(k)\}$ satisfies $\Pr\{\pi_1(k) = 1\} = \bar{\pi}$ and $\Pr\{\pi_1(k) = 0\} = 1 - \bar{\pi}$.

2.3. MN-RRLP under G-E Channel

For the standard RRP, only one node can access the network at each instant in a periodic sequence. Apparently, this transmission form does not consider the effect of packet dropout and neglects the impact of network condition. In this subsection, we propose a modified RRP such that the state signals from multiple sensors can be packaged into a packet and transmitted over a limited-bandwidth channel. To reflect the effect of network conditions, we introduce the number $p_{\theta(k-1)}$ of selected nodes with $1 \le p_{\theta(k-1)} \le n$.

For $\theta(k-2) = r$ and $\theta(k-1) = t$, we propose a channel-guided MN-RRLP, and $\varepsilon(k) \in \mathbb{H} \triangleq \{1, 2, \ldots, n\}$, termed a protocol token, denotes the first of the p_t selected sensor nodes at the current instant, whose update rule is

$$\varepsilon(k) = \begin{cases} 1, & \text{if } k = 1, \\ \operatorname{mod}(\varepsilon(k-1) + \bar{p}_0 - 1, n) + 1, & \text{if } k = 2, \\ \operatorname{mod}(\varepsilon(k-1) + p_r - 1, n) + 1, & \text{if } k \ge 3. \end{cases} \tag{4}$$

where $\operatorname{mod}(c, d)$ represents the non-negative remainder of the integer c divided by the positive integer d, and $\bar{p}_0$ is the number of selected nodes when $k = 1$. Further, $\bar{\varepsilon}_{i_t}(k) \in \mathbb{H}$ $(i_t \in \{1, 2, \ldots, p_t\})$ denotes the indices of all selected nodes as

$$\bar{\varepsilon}_{i_t}(k) = \begin{cases} \varepsilon(k), & \text{if } i_t = 1, \\ \operatorname{mod}(\bar{\varepsilon}_{i_t - 1}(k), n) + 1, & \text{if } 2 \le i_t \le p_t. \end{cases} \tag{5}$$

To elaborate the proposed MN-RRLP under G-E channels, we adopt the example depicted in Figure 2. Specifically, if the preceding channel mode is identified as the good mode, i.e., $\theta(k-1) = 1$, 4 sensor nodes are allowed to access the channel at the current instant, i.e., nodes 1, 2, 3, and 4. Correspondingly, when the channel operates in the bad mode at the current instant, i.e., $\theta(k) = -1$, only 2 sensor nodes are permitted to connect at the next instant, i.e., nodes 5 and 1. A core feature of this mechanism is that fewer sensor nodes are selected as network conditions degrade, which effectively prevents an excessive rise in packet dropout probability. Moreover, $\pi_{p_t}(k) \in \{0, 1\}$ is a random variable that indicates whether dropout of the p_t-node-length packet occurs when the channel is in the bad mode, satisfying the Bernoulli distribution as $\Pr\{\pi_{p_t}(k) = 1\} = \bar{\pi}^{p_t}$ and $\Pr\{\pi_{p_t}(k) = 0\} = 1 - \bar{\pi}^{p_t}$.

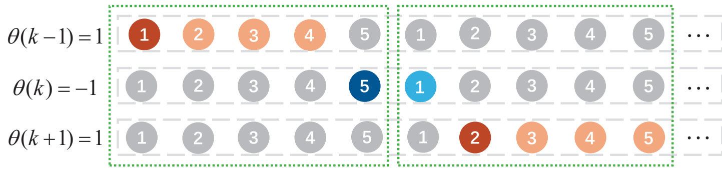

Figure 2. The diagram of the proposed MN-RRLP.

Remark 1. *The core innovation of the proposed MN-RRLP under the G-E channel lies in its active adaptation to real-time network conditions. Unlike the traditional RRP, which permits only a single node to access the network at each instant and inherently neglects the dynamic impact of network status, the MN-RRLP dynamically determines the number of selected nodes based on the channel mode. Nonetheless, because the communication protocol governs data scheduling at the forefront of network transmission, the node selection mechanism must inevitably rely on the previously obtained channel mode $\theta(k-1)$. The practical one-step-delayed mapping ensures that the protocol scales down the number of accessing sensor nodes when the network deteriorates into a bad mode, thereby proactively preventing a surge in packet dropout probability and alleviating bandwidth congestion.*

2.4. Encoding Strategy

In this subsection, we will design a dynamic encoding scheme involving a quantizer and an encoder under the G-E channel, where the quantized states are determined by the dynamic quantizer's parameter $\mu_j(k)$ ($j \in \mathbb{H}$). Under the G-E channel, the signal to be encoded consists of three parts: the channel mode $\theta(k) = v$, the transmitted system state $x_j(k)$, and the dynamic quantizer's parameter $\mu_j(k)$. The corresponding bit rates are denoted as T bits, X_j bits, and Y_j bits. The whole packet length is given as $\Re_j = T + X_j + Y_j$.

Part I: Firstly, a binary encoding scheme is designed for the channel mode $\theta(k) = v \in \{-1, 1\}$. The channel mode encoding function is

$$\tilde{\theta}(k) = \frac{v+1}{2} \in \{0, 1\}, \tag{6}$$

and the corresponding bit rate is

$$T = \lceil \log_2 2 \rceil = 1. \tag{7}$$

Part II: Subsequently, we discuss the quantization procedure for transmitted system state $x_j(k)$, which is quantized by the following dynamic uniform quantizer as

$$Q_{\mu_j(k)}(x_j(k)) \triangleq Q_j\left(\frac{x_j(k)}{\mu_j(k)}\right)\mu_j(k), \tag{8}$$

where $\mu_j(k) \in (0, 1]$ is the dynamic quantization parameter. The quantized state $Q_j(\frac{x_j(k)}{\mu_j(k)})$ in (8) is designated as

$$Q_j\left(\frac{x_j(k)}{\mu_j(k)}\right) \triangleq \begin{cases} -M_j, \text{ if } \frac{x_j(k)}{\mu_j(k)} \in (-\infty, -M_j) \\ -M_j + \frac{(2\beta_j-1)M_j}{\alpha_j}, \text{ if } \frac{x_j(k)}{\mu_j(k)} \in \beth_{\beta_j}, \\ M_j, \text{ if } \frac{x_j(k)}{\mu_j(k)} \in [M_j, \infty) \end{cases} \tag{9}$$

where the interval $[-M_j, M_j]$ is partitioned into α_j regions with $\alpha_j \triangleq 2^{X_j}$ and $\beth_{\beta_j} \triangleq [-M_j + \frac{2(\beta_j-1)M_j}{\alpha_j}, -M_j + \frac{2\beta_j M_j}{\alpha_j})$ with $\beta_j \in \{1, 2, \ldots, \alpha_j\}$. As such, if the zoomed state $\frac{x_j(k)}{\mu_j(k)}$ is located in the interval $[-M_j, M_j]$, then the quantization error satisfies

$$\left| Q_j\left(\frac{x_j(k)}{\mu_j(k)}\right) - \frac{x_j(k)}{\mu_j(k)} \right| \le \Delta_j \triangleq \frac{M_j}{\alpha_j}. \tag{10}$$

Thus, the encoding function for the quantized state $Q_j(\frac{x_j(k)}{\mu_j(k)})$ in (9) is given as

$$\tilde{x}_j(k) = \mathcal{F}_j\left(Q_j\left(\frac{x_j(k)}{\mu_j(k)}\right)\right) = \beta_j, \text{ if } \frac{x_j(k)}{\mu_j(k)} \in \beth_{\beta_j}. \tag{11}$$

Part III: Finally, we focus on the dynamic parameter $\mu_j(k)$, whose adjustment strategy is

$$\mu_j(k) = \begin{cases} \rho_j^{\iota_j(k)}, & \text{if } |x_j(k)| > M_j \underline{\mu}_j \\ \rho_j^{\bar{\iota}_j}, & \text{if } |x_j(k)| \leq M_j \underline{\mu}_j \end{cases}, \tag{12}$$

where $\rho_j \in (0,1)$ is a given constant; $\underline{\mu}_j \triangleq \min\{\mu_j(k)\} = \rho_j^{\bar{\iota}_j}$ is defined as the minimum dynamic parameter; and parameter $\iota_j(k)$ is given as

$$\iota_j(k) \triangleq \max_{\iota \in \mathbb{L}_j} \left\{\iota \big| |x_j(k)| \leq M_j \rho_j^{\iota}\right\} \tag{13}$$

with $\mathbb{L}_j \triangleq \{0, 1, \ldots, \bar{\iota}_j\}$ and $\bar{\iota}_j$ being given later. Moreover, when $|x_j(k)| > M_j \bar{\mu}_j$, we have

$$M_j \mu_j(k) \rho_j < |x_j(k)| \leq M_j \mu_j(k), \tag{14}$$

which implies that the quantizer (8) shall not saturate under the proposed adjustment strategy (12), that is,

$$|Q_{\mu_j(k)}(x_j(k)) - x_j(k)| \leq \Delta_j \mu_j(k), \tag{15}$$

for $x_j(k) \in [-M_j \mu_j(k), M_j \mu_j(k)]$. Thus, the encoding function for the corresponding dynamic parameter $\mu_j(k)$ in (12) is given as

$$\tilde{\mu}_j(k) = \mathcal{G}_j(\mu_j(k)) = \begin{cases} \aleph_j, & \text{if } M_j \rho_j^{\aleph_j+1} < |x_j(k)| \leq M_j \rho_j^{\aleph_j} \\ \bar{\iota}_j, & \text{if } |x_j(k)| \leq M_j \rho_j^{\bar{\iota}_j} \end{cases} \tag{16}$$

with $\tilde{\mu}_j(k) \in \mathbb{L}_j$, $\aleph_j \in \{0, 1, \ldots, \bar{\iota}_j - 1\}$, and $\bar{\iota}_j = 2^{Y_j} - 1$.

2.5. Decoding Strategy under G-E Channel

Firstly, the channel mode information is restored through the inverse mapping of (6) as follows:

$$\hat{\theta}(k) = 2\tilde{\theta}(k) - 1. \tag{17}$$

Subsequently, based on the update rule of the proposed multi-node protocol, if node j is selected and its data packet is successfully received, the value $x_j(k)$ of the jth sensor node is available to the controller. For nodes that have not been selected or whose data packets have not been successfully received, the controller can utilize their values from the previous instant. Accordingly, for $\theta(k) = v$, $\varepsilon(k) = q$, and $\theta(k-1) = t$, the available state of the jth sensor node for the controller is

$$\hat{x}_j(k) = \begin{cases} Q_{\mu_j(k)}(x_j(k)), & \text{if } \phi_{j,q,p_t} = 1, v = 1 \\ Q_{\mu_j(k)}(x_j(k)), & \text{if } \phi_{j,q,p_t} = 1, v = -1, \pi_{p_t}(k) = 1 \\ \hat{x}_j(k-1), & \text{otherwise} \end{cases} \tag{18}$$

where the flag signal $\phi_{j,q,p_t} = 1$ if there exists $\bar{\varepsilon}_{i_t}(k) = j$ for any $i_t \in \{1, 2, \ldots, p_t\}$ and $\phi_{j,q,p_t} = 0$ otherwise.

In order to compensate for possible lost states under the G-E channel, an input-holding strategy is adopted, and the corresponding decoding function is constructed as

$$\begin{aligned} \hat{x}_j(k) &= \mathcal{H}_j\big(\tilde{x}_j(k), \tilde{\mu}_j(k), \phi_{j,q,p_t}, v, \pi_{p_t}(k)\big) \\ &= \delta_1^v\big(\phi_{j,q,p_t}\vec{x}_j(k) + (1-\phi_{j,q,p_t})\hat{x}_j(k-1)\big) + \delta_{-1}^v\big(\phi_{j,q,p_t}\pi_{p_t}(k)\vec{x}_j(k) \\ &\quad + (1-\phi_{j,q,p_t}\pi_{p_t}(k))\hat{x}_j(k-1)\big) \end{aligned} \tag{19}$$

with $\vec{x}_j(k) \triangleq -M_j + \frac{(2\tilde{x}_j(k)-1)M_j}{\alpha_j}\rho_j^{\tilde{\mu}_j(k)}$. The Kronecker delta function $\delta_a^b = 1$ if $a = b$ and $\delta_a^b = 0$ otherwise.

Denote the encoding error as

$$e_j(k) = Q_{\mu_j(k)}(x_j(k)) - x_j(k). \tag{20}$$

Case I: For $M_j \underline{\mu}_j < |x_j(k)| \leq M_j \mu_j(k)$, (14) holds, and it follows from (10) and (14) that

$$|e_j(k)| \leq \Delta_j \mu_j(k) < \frac{\Delta_j |x_j(k)|}{M_j \rho_j} = \chi_j |x_j(k)| \tag{21}$$

with $\chi_j \triangleq \frac{1}{2^{X_j}\rho_j}$.

Case II: For $|x_j(k)| \leq M_j \underline{\mu}_j$, (14) does not hold. From (10), the encoding-error bound is

$$|e_j(k)| \leq \Delta_j \underline{\mu}_j = \frac{\rho_j^{2^{Y_j}-1} M_j}{2^{X_j}}. \tag{22}$$

Consequently, considering the dual effects of the proposed multi-node protocol and the G-E channel, the decoded state signal available at the controller side is expressed as

$$\begin{aligned} \hat{x}(k) = {} & \delta_1^v \Big(\Phi_{q,p_t}\big(x(k) + e(k)\big) + \big(I - \Phi_{q,p_t}\big)\hat{x}(k-1) \Big) + \delta_{-1}^v \Big(\Phi_{q,p_t}\pi_{p_t}(k)\big(x(k) + e(k)\big) \\ & + \big(I - \Phi_{q,p_t}\pi_{p_t}(k)\big)\hat{x}(k-1) \Big) \\ = {} & \digamma_{q,p_t}(k)(x(k) + e(k)) + (I - \digamma_{q,p_t}(k))\hat{x}(k-1) \end{aligned} \tag{23}$$

with $\hat{x}(k) \triangleq [\hat{x}_1(k), \hat{x}_2(k), \ldots, \hat{x}_n(k)]^\top$, $e(k) \triangleq [e_1(k), e_2(k), \ldots, e_n(k)]^\top$, $\digamma_{q,p_t}(k) \triangleq (\delta_1^v + \delta_{-1}^v \pi_{p_t}(k))\Phi_{q,p_t}$, and $\Phi_{q,p_t} \triangleq \mathrm{diag}\{\phi_{1,q,p_t}, \phi_{2,q,p_t}, \ldots, \phi_{n,q,p_t}\}$.

Remark 2. *It should be noted that the dynamic encoding-decoding mechanism in Sections 2.4 and 2.5 is designed not only for data transmission, but also to support the protocol adaptation. Specifically, by embedding the channel mode $\theta(k)$ into the transmitted packet and reconstructing it at the receiver, the controller side can obtain the updated channel information and feed back the one-step delayed mode $\theta(k-1)$ to the protocol. This enables the MN-RRLP to adaptively determine the number of accessing nodes according to channel conditions, thereby establishing a closed-loop interaction between the communication layer and the scheduling protocol, as discussed in Remark 1.*

3. Main Results

Based on the aforementioned problem formulation, this section will present the main research results of this paper, including the sliding mode controller design, stability analysis of the closed-loop system, reachability analysis of the sliding surface, and corresponding solving algorithms.

3.1. Controller Design

The following sliding function is designed as

$$s(k) = Rx(k), \tag{24}$$

where the sliding matrix R is selected as $R \triangleq \mho B^\top \in \mathbb{R}^{m \times n}$ with $\mho$ being a given constant. Then, we construct the sliding mode controller as

$$u(k) = K\hat{x}(k) - \bar{f}\mathrm{sgn}(\hat{s}(k)), \tag{25}$$

where the matrix $K \in \mathbb{R}^{m \times n}$ is the control gain that will be determined later, and $\hat{s}(k)$ is the sliding variable $s(k)$ in (24) with $x(k)$ replaced by $\hat{x}(k)$. Substituting (23) and (25) into the system (1), we have the closed-loop system as

$$x(k+1) = \big(\bar{A}(k) + BK\digamma_{q,p_t}(k)\big)x(k) + BK\digamma_{q,p_t}(k)e(k) + BK(I - \digamma_{q,p_t}(k))\hat{x}(k-1) + B\tilde{f}(k) \tag{26}$$

with $\bar{A}(k) \triangleq A + \tilde{A}(k)$ and $\tilde{f}(k) \triangleq f(k) - \bar{f}\mathrm{sgn}(\hat{s}(k))$.

3.2. Stability Analysis

The dominant objective of this subsection is to achieve EUB in mean square for the closed-loop system using the SMC method. For this purpose, we first introduce the following definition.

Definition 1. *For system (1), if there exist constants $\gamma \in (0,1)$, $c_1 > 0$, and $c_2 \geq 0$ such that $\mathcal{E}\{\|\eta(k)\|^2 | (\eta(0), v_0)\} \leq c_1 \|\eta(0)\|^2 \gamma^k + c_2$ for any $k > 0$, where $\eta(0) \in \mathbb{R}^n$ is the initial condition under the distribution $v_0 \in \{-1, 1\}$, then system (1) with $u(k) = 0$ achieves EUB in mean square, where γ is the decay rate and c_2 is the CUB of $\mathcal{E}\{\|\eta(k)\|^2\}$.*

Note that the closed-loop system (26) depends on the stochastic variables $\theta(k)$ and $\pi_{p_t}(k)$. Next, we will utilize the stochastic Lyapunov method to analyze the stability of the closed-loop system (26).

Theorem 1. *Given a constant $\gamma \in (0,1)$, if there exist matrices $P_v > 0$, $Q_v > 0$, K and scalars $\kappa_1 > 0$, $\varepsilon_1 > 0$, $\varpi > 0$, for $v \in \{-1,1\}$, satisfying*

$$K^\top B^\top \mathcal{P}_v BK \le \kappa_1 I, \;\; B^\top \mathcal{P}_v B \le \varepsilon_1 I, \;\; \mathcal{Q}_v \le \varpi I, \tag{27}$$

$$3\Gamma^\top \mathcal{P}_v \Gamma + 2\Upsilon^\top \mathcal{Q}_v \Upsilon + \Pi < 0 \tag{28}$$

with $\mathcal{P}_v \triangleq g_{v,-1}P_{-1} + g_{v,1}P_1$, $\mathcal{Q}_v \triangleq g_{v,-1}Q_{-1} + g_{v,1}Q_1$, $\Gamma \triangleq [\bar{A}(k) + BK\bar{F}_{q,p_t}, BK(I - \bar{F}_{q,p_t})]$, $\Upsilon \triangleq [\bar{F}_{q,p_t}, I - \bar{F}_{q,p_t}]$, $\bar{F}_{q,p_t} \triangleq (\delta_1^v + \delta_{-1}^v \bar{\pi}^{p_t})\Phi_{q,p_t}$, $\Pi \triangleq diag\{\nu_1\chi^2 - \gamma P_v, -\gamma Q_v\}$, $\nu_1 \triangleq 3\kappa_1 + 2\varpi$, and $\chi \triangleq diag\{\chi_1, \chi_2, \ldots, \chi_n\}$, then the closed-loop system (26) achieves EUB in mean square and the CUB of $\mathcal{E}\{\|\eta(k)\|^2\}$ is given as

$$c_2 = \frac{\psi_2}{(1-\gamma)\min\limits_{v\in\{-1,1\}}\{\lambda_{\min}(\mathbb{P}_v)\}} \tag{29}$$

with $\eta(k) \triangleq [x^\top(k), \hat{x}^\top(k-1)]^\top$, $\psi_2 \triangleq 3\varepsilon_1(1+\sqrt{m})^2\bar{f}^2 + \nu_1\underline{\mu}^\top\Delta^2\underline{\mu}$, $\mathbb{P}_v \triangleq diag\{P_v, Q_v\}$, $\Delta \triangleq diag\{\Delta_1, \Delta_2, \ldots, \Delta_n\}$, and $\underline{\mu} \triangleq [\underline{\mu}_1, \underline{\mu}_2, \ldots, \underline{\mu}_n]^\top$.

Proof. For channel mode $\theta(k) = v$, we choose the Lyapunov functional candidate as

$$V(\eta(k), v) = x^\top(k)P_v x(k) + \hat{x}^\top(k-1)Q_v\hat{x}(k-1). \tag{30}$$

For $\theta(k+1) = w$, it follows from (26) and (30) that

$$\begin{aligned}
&\mathcal{E}\{V(\eta(k+1), w)|(\eta(k), v)\} - \gamma V(\eta(k), v)\\
&= \mathcal{E}\{x^\top(k+1)P_v x(k+1)|(\eta(k), v)\} + \mathcal{E}\{\hat{x}^\top(k)Q_v\hat{x}(k)|(\eta(k), v)\}\\
&\quad - \gamma x^\top(k)P_v x(k) - \gamma\hat{x}^\top(k-1)Q_v\hat{x}(k-1).
\end{aligned} \tag{31}$$

Then, the first term on the right-hand side of (31) satisfies the following inequality:

$$\begin{aligned}
&\mathcal{E}\{x^\top(k+1)P_v x(k+1)|(\eta(k), v)\}\\
&\le 3\big((\bar{A}(k) + BK\bar{F}_{q,p_t})x(k) + BK(I - \bar{F}_{q,p_t})\hat{x}(k-1)\big)^\top \mathcal{P}_v\big((\bar{A}(k) + BK\bar{F}_{q,p_t})x(k)\\
&\quad + BK(I - \bar{F}_{q,p_t})\hat{x}(k-1)\big) + 3e^\top(k)(\bar{F}_{q,p_t})^\top K^\top B^\top \mathcal{P}_v BK\bar{F}_{q,p_t}e(k) + 3\tilde{f}^\top(k)B^\top\mathcal{P}_v B\tilde{f}(k).
\end{aligned} \tag{32}$$

From (21) and (22), we have

$$\|e(k)\|^2 \le x^\top(k)\chi^2 x(k) + \underline{\mu}^\top\Delta^2\underline{\mu}. \tag{33}$$

Noticing that $\|\mathrm{sgn}(\hat{s}(k))\| \le \sqrt{m}$ holds, we have $\|\tilde{f}(k)\| \le (1+\sqrt{m})\bar{f}$. And it is obvious that $\|\bar{F}_{q,p_t}\| \le 1$. Thus, by utilizing (27) and (33), we have

$$e^\top(k)(\bar{F}_{q,p_t})^\top K^\top B^\top \mathcal{P}_v BK\bar{F}_{q,p_t}e(k) \le \kappa_1(x^\top(k)\chi^2 x(k) + \underline{\mu}^\top\Delta^2\underline{\mu}), \tag{34}$$

$$\tilde{f}^\top(k)B^\top\mathcal{P}_v B\tilde{f}(k) \le \varepsilon_1(1+\sqrt{m})^2\bar{f}^2. \tag{35}$$

According to (32), (34), and (35), one has

$$\mathcal{E}\{x^\top(k+1)P_v x(k+1)|(\eta(k), v)\} \le 3\eta^\top(k)\Gamma^\top\mathcal{P}_v\Gamma\eta(k) + 3\kappa_1 x^\top(k)\chi^2 x(k) + \psi_1 \tag{36}$$

with $\psi_1 \triangleq 3\varepsilon_1(1+\sqrt{m})^2\bar{f}^2 + 3\kappa_1\underline{\mu}^\top\Delta^2\underline{\mu}$.

From (23) and (27), we have

$$\begin{aligned}
\mathcal{E}\{\hat{x}^\top(k)Q_v\hat{x}(k)|(\eta(k), v)\} &\le 2\eta^\top(k)\Upsilon^\top\mathcal{Q}_v\Upsilon\eta(k) + 2e^\top(k)(\bar{F}_{q,p_t})^\top\mathcal{Q}_v\bar{F}_{q,p_t}e(k)\\
&\le 2\eta^\top(k)\Upsilon^\top\mathcal{Q}_v\Upsilon\eta(k) + 2\varpi(x^\top(k)\chi^2 x(k) + \underline{\mu}^\top\Delta^2\underline{\mu}).
\end{aligned} \tag{37}$$

Substituting (36) and (37) into (31) yields

$$\mathcal{E}\{V(\eta(k+1),w)|(\eta(k),v)\}-\gamma V(\eta(k),v)\leq\eta^{\top}(k)(3\Gamma^{\top}\mathcal{P}_v\Gamma+2\Upsilon^{\top}\mathcal{Q}_v\Upsilon+\Pi)\eta(k)+\psi_2. \tag{38}$$

By combining (28) and applying mathematical expectation to both sides of (38), we have

$$\mathcal{E}\{V(\eta(k+1),w)\}-\gamma\mathcal{E}\{V(\eta(k),v)\}\leq\psi_2, \tag{39}$$

which means

$$\mathcal{E}\{V(\eta(k+1),w)\}-\mathcal{E}\{V(\eta(k),v)\}\leq(\gamma-1)\mathcal{E}\{V(\eta(k),v)\}+\psi_2. \tag{40}$$

Denoting $\bar{\gamma}\triangleq\frac{1}{\gamma}>1$, we have

$$\begin{aligned}&\bar{\gamma}^{k+1}\mathcal{E}\{V(\eta(k+1),w)\}-\bar{\gamma}^{k}\mathcal{E}\{V(\eta(k),v)\}\\&=\bar{\gamma}^{k+1}(\mathcal{E}\{V(\eta(k+1),w)\}-\mathcal{E}\{V(\eta(k),v)\})+\bar{\gamma}^{k}(\bar{\gamma}-1)\mathcal{E}\{V(\eta(k),v)\}\\&\leq\bar{\gamma}^{k}(\bar{\gamma}(\gamma-1)+(\bar{\gamma}-1))\mathcal{E}\{V(\eta(k),v)\}+\bar{\gamma}^{k+1}\psi_2\\&=\bar{\gamma}^{k+1}\psi_2.\end{aligned} \tag{41}$$

Next, by summing both sides of (41) over k from 0 to k_h-1, for $k_h\geq1$, we have

$$\mathcal{E}\{V(\eta(k_h),v_h)\}\leq\gamma^{k_h}\left(V(\eta(0),v_0)-\frac{\psi_2}{1-\gamma}\right)+\frac{\psi_2}{1-\gamma}, \tag{42}$$

from which we can derive that

$$\mathcal{E}\{\|\eta(k)\|^2\}\leq\frac{\max\limits_{v\in\{-1,1\}}\{\lambda_{\max}(\mathbb{P}_v)\}}{\min\limits_{v\in\{-1,1\}}\{\lambda_{\min}(\mathbb{P}_v)\}}\|\eta(0)\|^2\gamma^k+\frac{\psi_2}{(1-\gamma)\min\limits_{v\in\{-1,1\}}\{\lambda_{\min}(\mathbb{P}_v)\}}. \tag{43}$$

Therefore, according to Definition 1, the closed-loop system (26) achieves EUB in mean square, and it is straightforward to calculate the CUB of $\mathcal{E}\{\|\eta(k)\|^2\}$ as c_2. □

3.3. Reachability Analysis

After proving EUB of the controlled system, this subsection will further analyze how to drive the system state into the specified sliding surface neighborhood, that is, the reachability of the sliding surface.

Theorem 2. *Given a constant $\gamma\in(0,1)$, if there exist matrices $P_v>0$, $Q_v>0$, $W_v>0$, K, and scalars $\kappa_1>0$, $\kappa_2>0$, $\varepsilon_1>0$, $\varepsilon_2>0$, $\varpi>0$, for $v\in\{-1,1\}$, satisfying (27) and*

$$K^{\top}B^{\top}R^{\top}\mathcal{W}_vGBK\leq\kappa_2 I,\ \ B^{\top}R^{\top}\mathcal{W}_vGB\leq\varepsilon_2 I, \tag{44}$$

$$3\Gamma^{\top}\mathcal{P}_v\Gamma+2\Upsilon^{\top}\mathcal{Q}_v\Upsilon+3\tilde{\Gamma}^{\top}\mathcal{W}_v\tilde{\Gamma}+\tilde{\Pi}<0 \tag{45}$$

with $\mathcal{W}_v\triangleq g_{v,-1}W_{-1}+g_{v,1}W_1$, $\tilde{\Pi}\triangleq diag\{\nu_2\chi^2-\gamma P_v,-\gamma Q_v\}$, $\tilde{\Gamma}\triangleq[R(\bar{A}(k)+BK\bar{F}_{q,p_t}),RBK(I-\bar{F}_{q,p_t})]$, and $\nu_2\triangleq3(\kappa_1+\kappa_2)+2\varpi$, then the system states can be steered into the domain O near the designated sliding surface $s(k)=0$ as

$$O=\{s(k)|\|s(k)\|\leq\sqrt{\frac{\psi_4}{\gamma\min\limits_{v\in\{-1,1\}}\{\lambda_{\min}(W_v)\}}}\} \tag{46}$$

with $\psi_4\triangleq3(\varepsilon_1+\varepsilon_2)(1+\sqrt{m})^2\bar{f}^2+\nu_2\underline{\mu}^{\top}\Delta^2\underline{\mu}$.

Proof. The Lyapunov functional candidate is selected as

$$U(\eta(k),v)=V(\eta(k),v)+s^{\top}(k)W_vs(k). \tag{47}$$

Following the same approach as in (31), we can derive

$$\begin{aligned}&\mathcal{E}\{U(\eta(k+1),w)|(\eta(k),v)\}-\gamma U(\eta(k),v)\\&=\mathcal{E}\{V(\eta(k+1),w)|(\eta(k),v)\}-\gamma V(\eta(k),v)+\mathcal{E}\{s^{\top}(k+1)W_vs(k+1)|(\eta(k),v)\}-\gamma s^{\top}(k)W_vs(k).\end{aligned} \tag{48}$$

According to (24) and (26), one has

$$s(k+1) = R(\bar{A}(k) + BK\bar{\digamma}_{q,p_t})x(k) + RBK\bar{\digamma}_{q,p_t}e(k) + RBK(I - \bar{\digamma}_{q,p_t})\hat{x}(k-1) + RB\tilde{f}(k). \tag{49}$$

Similar to the derivation process of (32)–(36), it follows from (44) that

$$\mathcal{E}\{s^\top(k+1)W_v s(k+1)|(\eta(k),v)\} \leq 3\eta^\top(k)\tilde{\Gamma}^\top \mathcal{W}_v\tilde{\Gamma}\eta(k) + 3\kappa_2 x^\top(k)\chi^2 x(k) + \psi_3 \tag{50}$$

with $\psi_3 \triangleq 3\varepsilon_2(1+\sqrt{m})^2\bar{f}^2 + 3\kappa_2\underline{\mu}^\top\Delta^2\underline{\mu}$. Furthermore, substituting (50) into (48) yields

$$\begin{aligned}&\mathcal{E}\{U(\eta(k+1),w)|(\eta(k),v)\} - \gamma U(\eta(k),v)\\ &\leq \eta^\top(k)(3\Gamma^\top\mathcal{P}_v\Gamma + 2\Upsilon^\top\mathcal{Q}_v\Upsilon + 3\tilde{\Gamma}^\top\mathcal{W}_v\tilde{\Gamma} + \tilde{\Pi})\eta(k) + \psi_4 - \gamma\min_{v\in\{-1,1\}}\{\lambda_{\min}(W_v)\}\|s(k)\|^2.\end{aligned} \tag{51}$$

Observe that if (45) holds, we have $\mathcal{E}\{U(\eta(k+1),w) \mid (\eta(k),v)\} - \gamma U(\eta(k),v) < 0$ from (51) when the system states are outside the sliding domain O, that is, $\|s(k)\| > \sqrt{\frac{\psi_4}{\gamma\min_{v\in\{-1,1\}}\{\lambda_{\min}(W_v)\}}}$. Taking the mathematical expectation on both sides, we get $\mathcal{E}\{U(\eta(k+1),w)\} < \gamma\mathcal{E}\{U(\eta(k),v)\}$ indicating that the Lyapunov functional $U(\eta(k),v)$ is monotonically decreasing in mean square out of the domain O. Consequently, the system states can be steered into the domain O near the designated sliding surface $s(k)=0$ in mean square. It is clear that the sliding domain O is affected by the minimum quantization error $\Delta\underline{\mu}$ and the Lyapunov matrix W_v. □

3.4. Solving Algorithm

To ensure the feasibility of theoretical results, this subsection transforms the aforementioned stability and reachability conditions into a set of LMIs that can be numerically solved, and proposes a specific controller gain solving algorithm.

Theorem 3. *Given a constant $\gamma \in (0,1)$, if there exist matrices $\bar{P}_v > 0$, $Q_v > 0$, $\bar{W}_v > 0$, K, and scalars $\kappa_1 > 0$, $\kappa_2 > 0$, $\varepsilon_1 > 0$, $\varepsilon_2 > 0$, $\varpi > 0$, $\vartheta > 0$, for $v \in \{-1,1\}$, satisfying*

$$\begin{bmatrix}-\kappa_1 I & * & *\\ \sqrt{g_{v,-1}}BK & -\bar{P}_{-1} & *\\ \sqrt{g_{v,1}}BK & 0 & -\bar{P}_1\end{bmatrix} \leq 0, \begin{bmatrix}-\varepsilon_1 I & * & *\\ \sqrt{g_{v,-1}}B & -\bar{P}_{-1} & *\\ \sqrt{g_{v,1}}B & 0 & -\bar{P}_1\end{bmatrix} \leq 0, \begin{bmatrix}-\varpi I & * & *\\ \sqrt{g_{v,-1}}Q_{-1} & -Q_{-1} & *\\ \sqrt{g_{v,1}}Q_1 & 0 & -Q_1\end{bmatrix} \leq 0, \tag{52}$$

$$\begin{bmatrix}-\kappa_2 I & * & *\\ \sqrt{g_{v,-1}}RBK & -\bar{W}_{-1} & *\\ \sqrt{g_{v,1}}RBK & 0 & -\bar{W}_1\end{bmatrix} \leq 0, \begin{bmatrix}-\varepsilon_2 I & * & *\\ \sqrt{g_{v,-1}}RB & -\bar{W}_{-1} & *\\ \sqrt{g_{v,1}}RB & 0 & -\bar{W}_1\end{bmatrix} \leq 0, \tag{53}$$

$$\begin{bmatrix}\Omega_{11} & * & * & *\\ \Omega_{21} & \Omega_{22} & * & *\\ 0 & \Omega_{32} & -\vartheta I & *\\ \Omega_{41} & 0 & 0 & -\nu_2 I\end{bmatrix} < 0 \tag{54}$$

with $\Omega_{11} \triangleq diag\{\gamma(\bar{P}_v - 2I) + \vartheta H^\top H, -\gamma Q_v\}$,

$$\Omega_{21} \triangleq \begin{bmatrix}\sqrt{g_{v,-1}}(A + BK\bar{\digamma}_{q,p_t}) & \sqrt{g_{v,-1}}BK(I - \bar{\digamma}_{q,p_t})\\ \sqrt{g_{v,1}}(A + BK\bar{\digamma}_{q,p_t}) & \sqrt{g_{v,1}}BK(I - \bar{\digamma}_{q,p_t})\\ \sqrt{g_{v,-1}}Q_{-1}\bar{\digamma}_{q,p_t} & \sqrt{g_{v,-1}}Q_{-1}(I - \bar{\digamma}_{q,p_t})\\ \sqrt{g_{v,1}}Q_1\bar{\digamma}_{q,p_t} & \sqrt{g_{v,1}}Q_1(I - \bar{\digamma}_{q,p_t})\\ \sqrt{g_{v,-1}}R(A + BK\bar{\digamma}_{q,p_t}) & \sqrt{g_{v,-1}}RBK(I - \bar{\digamma}_{q,p_t})\\ \sqrt{g_{v,1}}R(A + BK\bar{\digamma}_{q,p_t}) & \sqrt{g_{v,1}}RBK(I - \bar{\digamma}_{q,p_t})\end{bmatrix},$$

$\Omega_{22} \triangleq diag\{-\frac{\bar{P}_{-1}}{3}, -\frac{\bar{P}_1}{3}, -\frac{Q_{-1}}{2}, -\frac{Q_1}{2}, -\frac{\bar{W}_{-1}}{3}, -\frac{\bar{W}_1}{3}\}$, $\Omega_{32} \triangleq [E^\top, E^\top, 0, 0, E^\top R^\top, E^\top R^\top]$, and $\Omega_{41} \triangleq [\nu_2\chi, 0]$, then the closed-loop system (26) can achieve EUB in mean square and the system states can be steered into the domain O near the designated sliding surface $s(k)=0$ in mean square.

Proof. Define $\bar{P}_v \triangleq P_v^{-1}$ and $\bar{W}_v \triangleq W_v^{-1}$. It is obvious that $\tilde{\Pi} > \Pi$ and $\tilde{\Gamma}^\top\mathcal{W}_v\tilde{\Gamma} > 0$ hold, which means that (28) in Theorem 1 can be guaranteed by (54). And by using Schur complement, (27) can be ensured by (52). Following derivations similar to (30)–(39) in Theorem 1, Lyapunov functional $V(\eta(k),v)$ is attenuated, unless the current state is inside the CUB c_2. Similarly, the designated sliding surface $s(k)=0$ can be reached. □

4. Bit Rate Intelligent Pre-allocation

Under the premise of a given decay rate γ, optimizing the steady-state performance of the system becomes a key objective in controller design. According to Definition 1, the steady-state accuracy of the system is determined by the CUB c_2. Clearly, minimizing c_2 can effectively enhance the steady-state control precision of the system, resulting in a smaller fluctuation range and stronger robustness after convergence.

To be specific, the expression for c_2 includes the encoding-error term $\underline{\mu}^\top \Delta^2 \underline{\mu}$, with $\Delta_j = \frac{M_j}{2^{X_j}}$ and $\underline{\mu}_j = \rho_j^{2^{Y_j}-1}$, which indicates that c_2 is directly influenced by the bit rates X_j and Y_j. Therefore, by intelligently pre-allocating the bit rates X_j and Y_j under the constraint of the total bit rate $\Re_j = T + X_j + Y_j$, minimizing c_2 not only has a clear physical significance, but is also mathematically feasible, and can be transformed into an optimization problem under LMI constraints.

Corollary 1. *Given a constant $\gamma \in (0,1)$, if there exist matrices $\bar{P}_v > 0$, $Q_v > 0$, $\bar{W}_v > 0$, K, and scalars $\kappa_1 > 0$, $\kappa_2 > 0$, $\varepsilon_1 > 0$, $\varepsilon_2 > 0$, $\varpi > 0$, $\vartheta > 0$, for $v \in \{-1, 1\}$, such that the following minimization problem is feasible:*

$$\textbf{\textit{OP:}} \ \min_{X_j, Y_j} \ c_2, \tag{55}$$

$$\textit{subject to } (52)\text{–}(54) \textit{ and } \Re_j = T + X_j + Y_j \ (j \in \mathbb{H}),$$

then the closed-loop system (26) achieves EUB in mean square and the optimal allocation scheme for X_j, Y_j can be obtained.

It is noted that X_j, Y_j are positive integers, which leads to an integer programming problem. When integrated with the LMI-based optimization problem (55), traditional integer programming methods, such as branch and bound, cutting plane, and implicit enumeration, are inadequate for efficiently solving such mixed-integer programming problems. With the progress in artificial intelligence technologies, a growing number of heuristic algorithms have emerged and are extensively applied to optimization problems in control theory, including swarm intelligence algorithms, evolutionary algorithms, and learning-based algorithms. Among these, the SAA, as a stochastic optimization method based on a Monte-Carlo iterative solution strategy, exhibits notable advantages in addressing the aforementioned combinatorial optimization problems.

In the subsequent discussion, by utilizing SAA to solve the mixed-integer programming problem (55), we propose an allocation and optimization scheme for X_j, Y_j. Specifically, the following Algorithm 1 presents the detailed scheme.

Algorithm 1 SAA-LMI-Crossed Optimization Scheme

Step 1: Set SAA parameters: initial temperature $\mathbf{T}_0$, terminal temperature $\mathbf{T}_t < \mathbf{T}_0$, cooling factor $0 < \mathbf{C}_f < 1$, the number of iterations $\mathbf{N}$, iteration counter $\mathbf{L}$, increment threshold $\hbar$.

Step 2: Initialize temperature: $\mathbf{T} = \mathbf{T}_0$.

Step 3: Generate initial solution: Let $\mathbf{L} = 0$. Under temperature $\mathbf{T}$, for $X_j, Y_j \in \mathrm{INT}_{[1, \Re_j - 1]}$, randomly generate integer initial solution $\{X_1^{(0)}, Y_1^{(0)}, \ldots, X_n^{(0)}, Y_n^{(0)}\}$. Then, calculate the corresponding initial $c_2^{(0)}$.

Step 4: Iterate:

1. Update the iteration counter: $\mathbf{L} = \mathbf{L} + 1$.
2. Update solution: By using integer stochastic disturbance, generate candidate solution $\{X_1^{(\mathbf{L})}, Y_1^{(\mathbf{L})}, \ldots, X_n^{(\mathbf{L})}, Y_n^{(\mathbf{L})}\}$. Then, calculate $c_2^{(\mathbf{L})}$. If $c_2^{(\mathbf{L})} < c_2^{(\mathbf{L}-1)}$, choose the candidate solution as new solution; otherwise, update the solution with the probability $e^{-\frac{c_2^{(\mathbf{L})} - c_2^{(\mathbf{L}-1)}}{\mathbf{T}^{\mathbf{L}}}}$.
3. Exit condition: $\mathbf{L} = \mathbf{N}$.

Step 5: Update temperature: $\mathbf{T} = \mathbf{C}_f \mathbf{T}$.

Step 6: Termination conditions: If $\mathbf{T} < \mathbf{T}_t$ or $|c_2^{(\mathbf{L})} - c_2^{(\mathbf{L}-1)}| < \hbar$, terminate and record the current solution as the optimal solution $\{X_1^{(\mathbf{M})}, Y_1^{(\mathbf{M})}, \ldots, X_n^{(\mathbf{M})}, Y_n^{(\mathbf{M})}\}$; otherwise, return to **Step 3**.

Step 7: Under the optimal allocation scheme $\{X_1^{(\mathbf{M})}, Y_1^{(\mathbf{M})}, \ldots, X_n^{(\mathbf{M})}, Y_n^{(\mathbf{M})}\}$, calculate the controller gains $K^{(\mathbf{M})}$, and then obtain the corresponding controller.

Remark 3. *A significant theoretical breakthrough of this work lies in establishing the direct mathematical relationship between the CUB and the bit rates of states and dynamic parameters. In standard networked control* *designs, the joint design of network resource allocation and controller parameters often encounters highly nonlinear constraints, causing steady-state accuracy and bandwidth limitations to be analyzed independently. In this paper, the expression for the CUB c_2 incorporates encoding error terms that are directly determined by the pre-allocated bit rates X_j and Y_j. Through this analytical framework, maximizing control precision is mapped onto a mixed-integer programming problem subject to bandwidth limits. This co-design perspective enables the optimization algorithm to perform adaptive bit allocation, sparing more bandwidth resources for critical states to fundamentally minimize the steady-state quantization errors.*

5. Illustrative Example

In this section, a numerical example is provided to demonstrate the effectiveness of the proposed SMC strategy. Consider the NCS (1) characterized by the following matrices:

$$A = \begin{bmatrix} 0.1862 & 0.2747 & -0.1489 & 0.1023 \\ -0.1113 & 0.3459 & 0.4155 & -0.1533 \\ 0.2761 & -0.1044 & 0.3056 & 0.4117 \\ -0.4141 & 0.0875 & -0.2787 & 0.1903 \end{bmatrix}, \; B = \begin{bmatrix} 0.4378 & -0.2274 & 0.2344 & -0.2708 \end{bmatrix}^\top.$$

The norm-bounded parameter uncertainty is assumed to be $\tilde{A}(k) = EL(k)H$, where $E = [0.01\ \ 0.02\ \ -0.01\ \ 0.03]^\top$, $L(k) = \sin(k)$, and $H = [0.02\ \ -0.1\ \ 0.3\ \ 0.1]$. The external disturbance is defined as $f(k) = 0.01\cos(k)$. In addition, the decay rate and sliding mode parameter are chosen as $\gamma = 0.95$ and $\mho = 0.7$, respectively. Consequently, the sliding matrix is determined as $R = \mho B^\top = [0.3065\ \ -0.1592\ \ 0.1641\ \ -0.1896]$.

Next, the transition probabilities $g_{t,v}$ $(t, v \in \{-1, 1\})$ for the channel mode $\theta(k)$ within the communication network are set to $g_{-1,-1} = 0.45$, $g_{-1,1} = 0.55$, $g_{1,-1} = 0.35$, and $g_{1,1} = 0.65$. It follows that the stationary distribution of the Markov chain $\{\theta(k)\}$ is $\bar{\omega} = [0.4375\ \ 0.5625]$. Under single-node transmission, the probability of the channel being in bad mode without packet dropout is $\bar{\pi} = 0.6$. Based on the mechanism depicted in Figure 2, the zero-packet-loss probability in bad mode under the multi-node scheme is calculated as $\bar{\pi}^{p_t} = 0.6^2 = 0.36$. Furthermore, the quantization ranges are assigned as $M_1 = 0.8$, $M_2 = 0.6$, $M_3 = 0.7$, and $M_4 = 0.9$, with the dynamic quantization constants ρ_j $(j = 1, 2, 3, 4)$ set as $\rho_1 = 0.5$, $\rho_2 = 0.3$, $\rho_3 = 0.8$, and $\rho_4 = 0.6$. Referring to (6), we obtain $T = 1$. For a total bit rate $\Re_j = 14$, the remaining bits for the system state and dynamic parameters are $X_j + Y_j = 13$. Finally, the SAA parameters for bit-rate pre-allocation are specified as $\mathbf{T}_0 = 100$, $\mathbf{T}_t = 0.1$, $\mathbf{C}_f = 0.9$, $\mathbf{N} = 10$, and $\hbar = 10^{-8}$.

Applying Algorithm 1 yields the optimal bit-allocation scheme $\{X_1^{(\mathbf{M})}, Y_1^{(\mathbf{M})}, X_2^{(\mathbf{M})}, Y_2^{(\mathbf{M})}, X_3^{(\mathbf{M})}, Y_3^{(\mathbf{M})}, X_4^{(\mathbf{M})}, Y_4^{(\mathbf{M})}\} = \{7, 6, 8, 5, 9, 4, 12, 1\}$. By solving the LMIs (52)–(54) with this scheme, the controller gain is found to be $K = [-0.1274\ \ 0.0403\ \ -0.0541\ \ -0.1033]$. Simulation results, initialized at $x(0) = [-2\ \ 1\ \ -1\ \ 2]^\top$, are illustrated in Figure 3. As shown in Figure 3a, the state trajectories show that the closed-loop system (26) achieves EUB via the proposed SMC scheme under the G-E channel and MN-RRLP. The evolution curves of the sliding variable and control signal are displayed in Figure 3b and 3c, respectively, verifying that the system states effectively reach the sliding domain around $s(k) = 0$. Lastly, Figure 3d reveals that the dynamic quantization parameters adaptively adjust according to system state fluctuations until convergence within the CUB is achieved.

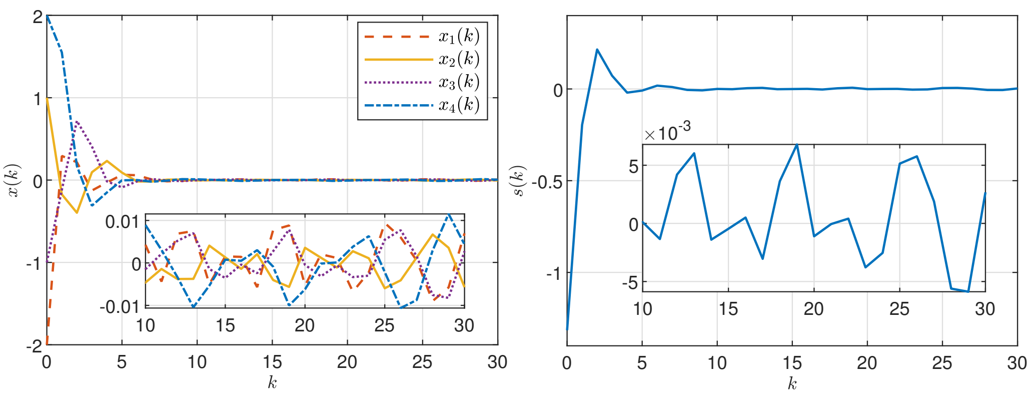

(a) System state $x(k)$. **(b)** Sliding variable $s(k)$.

Figure 3. *Cont.*

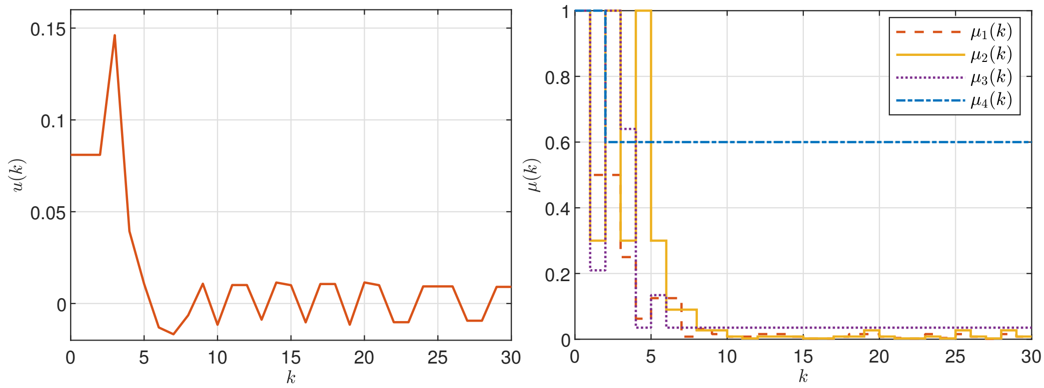

(c) Control signal $u(k)$.

(d) Dynamic parameter $\mu(k)$.

Figure 3. Simulation results under optimal bit-rate allocation.

To verify the superiority of the proposed channel-guided MN-RRLP under G-E channels, Figure 4 compares the system performance between the proposed MN-RRLP and the traditional single-node RRP. It is observed from the cumulative sliding variable $\sum_{i=1}^{k} s^2(i)$ in Figure 4a and the cumulative system state norm $\sum_{i=1}^{k} \|x(i)\|^2$ in Figure 4b that the steady-state convergence values of the curves representing MN-RRLP are lower than those of the traditional RRP. This indicates that the sliding variable and system states converge more stably and remain within the sliding domain and CUB, respectively. The above results demonstrate that MN-RRLP effectively mitigates the adverse impact of packet dropout on global regulation quality by dynamically adjusting the number of accessing nodes, thereby significantly improving the steady-state performance of the closed-loop system under network fluctuations.

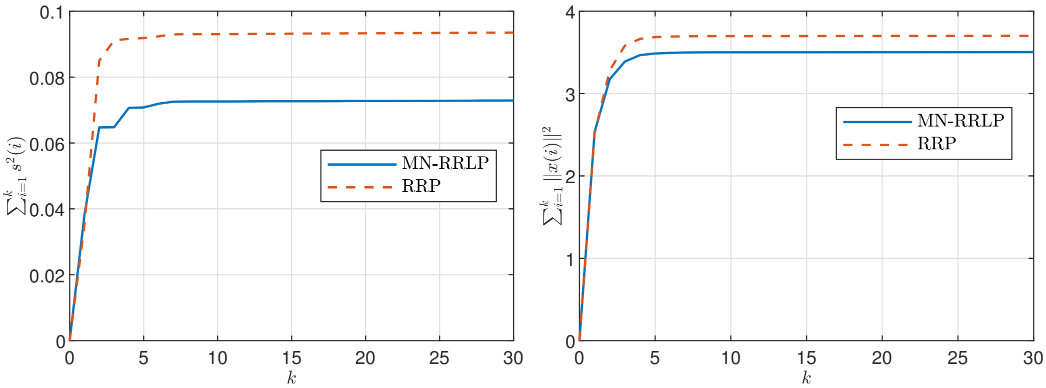

(e) Sliding variable $\sum_{i=1}^{k} s^2(i)$.

(f) State norm $\sum_{i=1}^{k} \|x(i)\|^2$.

Figure 4. Simulation results under MN-RRLP and RRP.

To highlight the improvement in steady-state control precision achieved by the dynamic quantization encoding-decoding mechanism, Figure 5 provides a comparison between the proposed dynamic coding and traditional static coding where the quantization parameter remains constant at $\mu \equiv 1$. Figure 5a depicts the evolution of the real-time quantization level $2\Delta(k)$. The quantization level of the proposed method contracts adaptively as system states converge, whereas the quantization level for static coding remains at a higher constant level due to the fixed quantization range. This coarse-to-fine dynamic adjustment capability directly influences the smoothness of control signals. As shown by the cumulative control energy consumption $\sum_{i=2}^{k}(u(i) - u(i-1))^2$ in Figure 5b, the cumulative energy consumption of the dynamic coding scheme is smaller than that of the static coding scheme. This further validates the advantages of the designed dynamic parameter adjustment mechanism in eliminating quantization errors and suppressing sliding mode chattering.

Under the constraint of strictly limited total bandwidth resources, Figure 6 compares the SAA-based intelligent bit-rate pre-allocation scheme with the traditional uniform allocation scheme. Figure 6a illustrates the decay of the dynamic quantization parameter norm $\|\mu(k)\|$ in a logarithmic coordinate system. It is observed that the dynamic parameters under the SAA-optimized scheme exhibit larger values and converge to lower levels, which implies that fewer bit rates are required for transmitting these parameters, thereby sparing more bandwidth resources for encoding the system states to enhance overall control precision. To intuitively reflect the rationality of resource allocation,

Figure 6b presents the global cumulative error $\sum_{i=1}^{k}\|x(i)-\hat{x}(i)\|$. Compared with the uniform allocation scheme that blindly averages resources, the SAA scheme performs optimized nonuniform bit allocation to reduce the overall cumulative system deviation, resulting in a gap between the two curves. This result fully proves that transforming the minimization of the CUB into a mixed-integer programming problem and using SAA to solve the problem intelligently can maximize the utilization of limited network bits and obtain the optimal global quantization fidelity.

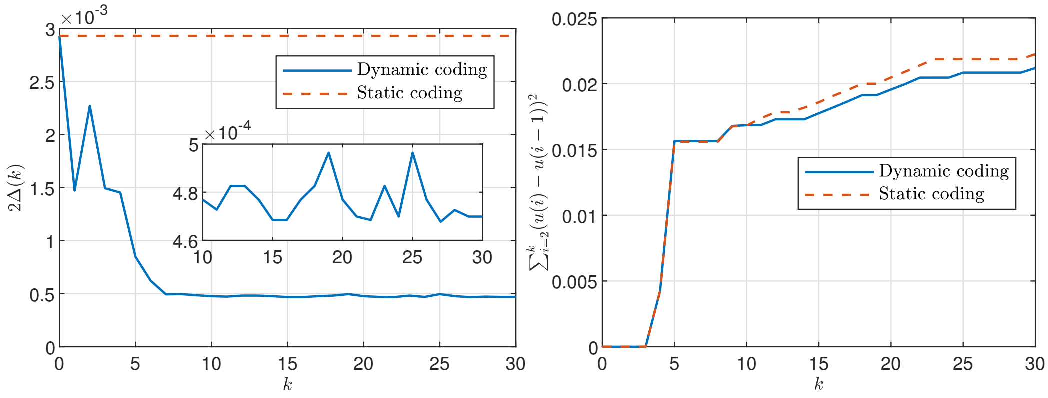

(a) Quantization level $2\Delta(k)$.

(b) Control energy consumption $\sum_{i=2}^{k}(u(i)-u(i-1))^2$.

Figure 5. Simulation results under dynamic and static coding.

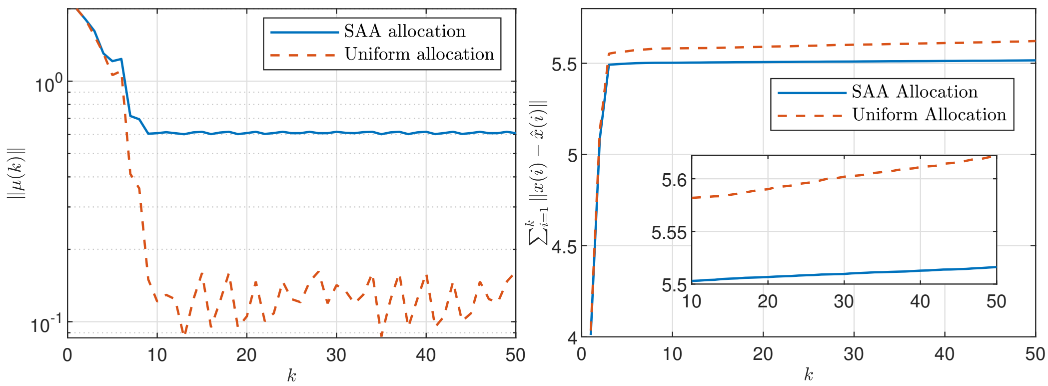

(a) Dynamic parameter norm $\|\mu(k)\|$.

(b) System error $\sum_{i=1}^{k}\|x(i)-\hat{x}(i)\|$.

Figure 6. Simulation results under SAA and uniform allocation.

6. Conclusions

This paper has established a joint design framework of dynamic quantization encoding-decoding mechanism and SMC law for NCSs over G-E channels. By introducing the channel-guided MN-RRLP, the proposed framework overcomes the limitations of single-node scheduling by adaptively decreasing the number of selected nodes during network deterioration. The integration of the dynamic encoding-decoding mechanism with SMC not only ensures robustness against external perturbations but also effectively addresses the constraints of total bit rates. By transforming the minimization of the CUB into an LMI-constrained mixed-integer programming problem, SAA is efficiently utilized to achieve intelligent bit-rate pre-allocation. Ultimately, the proposed comprehensive strategy theoretically guarantees the EUB of the system in mean square and provides an effective optimal solution for enhancing the steady-state control precision of resource-constrained NCSs.

Author Contributions: P.Z.: conceptualization, methodology, writing—original draft preparation, software, validation; Z.C.: data curation, validation, writing—reviewing and editing, supervision; C.P.: visualization, investigation, supervision.

Funding: This work was supported in part by the National Natural Science Foundation of China under Grants 62533016, and 62573279; in part by the Shanghai Natural Science Foundation under Grant 24ZR1454700; in part by the Natural Science Foundation of Shandong Province under Grant ZR2025MS1113.

Data Availability Statement: Not applicable.

Conflicts of Interest: The authors declare no conflict of interest.

Use of AI and AI-Assisted Technologies: No AI tools were utilized for this paper.

References

1. Zou, L.; Wang, Z.; Shen, B.; et al. Encryption-Decryption-Based State Estimation with Multirate Measurements against Eavesdroppers: A Recursive Minimum-Variance Approach. *IEEE Trans. Autom. Control* **2023**, *68*, 8111–8118.
2. Song, B.; Shang, Z.; Wang, Z. Trajectory tracking control of omni-directional mobile robots: A HOFA-LESO based approach. *Robot. Auton. Syst.* **2026**, *202*, 105492.
3. Peng, S.; Zhang, Z.; Deng, R.; et al. Localizing False Data Injection Attacks in Smart Grid: A Spectrum-Based Neural Network Approach. *IEEE Trans. Smart Grid* **2023**, *14*, 3723–3737.
4. Lou, X.; Yang, X.; Sun, J.; et al. Optimization Scheduling Strategy for Coal Railway Integrated Energy Systems. *Energies* **2025**, *18*, 4534.
5. Li, C.; Liu, Y.; Gao, M.; et al. Fault-tolerant formation consensus control for time-varying multi-agent systems with stochastic communication protocol. *Int. J. Netw. Dyn. Intell.* **2024**, *3*, 100004.
6. Song, B.; Zhao, S.; Wang, Z.; et al. DAF-DETR: A dynamic adaptation feature transformer for enhanced object detection in unmanned aerial vehicles. *Knowl.-Based Syst.* **2025**, *323*, 113760.
7. Wang, X.; Sun, Y.; Ding, D. Adaptive Dynamic Programming for Networked Control Systems under Communication Constraints: A Survey of Trends and Techniques. *Int. J. Netw. Dyn. Intell.* **2022**, *1*, 85–98.
8. Zhang, X.M.; Han, Q.L.; Ge, X. A novel approach to H_∞ performance analysis of discrete-time networked systems subject to network-induced delays and malicious packet dropouts. *Automatica* **2022**, *136*, 110010.
9. Zhang, D.; Han, Q.L.; Zhang, X.M. Network-Based Modeling and Proportional-Integral Control for Direct-Drive-Wheel Systems in Wireless Network Environments. *IEEE Trans. Cybern.* **2020**, *50*, 2462–2474.
10. Wu, J.; Peng, C.; Zhang, J.; et al. A Sampled-Data-Based Secure Control Approach for Networked Control Systems under Random DoS Attacks. *IEEE Trans. Cybern.* **2024**, *54*, 4841–4851.
11. Liu, D.; Wang, Z.; Liu, Y.; et al. Recursive State Estimation for Stochastic Complex Networks under Round-Robin Communication Protocol: Handling Packet Disorders. *IEEE Trans. Netw. Sci. Eng.* **2021**, *8*, 2455–2467.
12. Liu, J.; Gong, E.; Zha, L.; et al. Observer-Based Security Fuzzy Control for Nonlinear Networked Systems under Weighted Try-Once-Discard Protocol. *IEEE Trans. Fuzzy Syst.* **2023**, *31*, 3853–3864.
13. Zou, L.; Wang, Z.; Hu, J.; et al. On H_∞ finite-horizon filtering under stochastic protocol: Dealing with high-rate communication networks. *IEEE Trans. Autom. Control* **2017**, *62*, 4884–4890.
14. Chen, H.; Wang, Z.; Liang, J.; et al. State Estimation for Stochastic Time-Varying Boolean Networks. *IEEE Trans. Autom. Control* **2020**, *65*, 5480–5487.
15. Chen, H.; Wang, Z.; Shen, B.; et al. Distributed Recursive Filtering over Sensor Networks with Nonlogarithmic Sensor Resolution. *IEEE Trans. Autom. Control* **2022**, *67*, 5408–5415.
16. Zhao, H.; Wang, W.; He, W. Dynamic event-triggered sliding mode control for T-S fuzzy switched systems with multi-node stochastic communication protocols. *Appl. Math. Comput.* **2026**, *523*, 130024.
17. Yang, S.; Caballero-Aguila, R.; Hu, J.; et al. Secure Tobit filtering for multi-rate nonlinear systems under multi-node random access protocol: A Paillier encryption-decryption mechanism. *Inf. Fusion* **2026**, *130*, 104146.
18. Hu, Y.; Kwon, O.M.; Lee, S.H. H_∞ control for interval type-2 fuzzy singularly perturbed systems with multi-node round-robin protocol and packet dropouts. *Fuzzy Sets Syst.* **2025**, *500*, 109202.
19. Zhang, P.; Kao, Y.; Hu, J.; et al. Robust observer-based sliding mode H_∞ control for stochastic Markovian jump systems subject to packet losses. *Automatica* **2021**, *130*, 109665.
20. Wu, Y.; Zhao, X.; Shen, Z.; et al. Stability Analysis of Connected Vehicle Platoons with Markovian Packet Losses. *IEEE Trans. Intell. Transp. Syst.* **2025**, *26*, 3155–3169.
21. Ding, D.; Wang, Z.; Han, Q.L.; et al. Recursive Secure Filtering Over Gilbert-Elliott Channels in Sensor Networks: The Distributed Case. *IEEE Trans. Signal Inf. Process. Netw.* **2021**, *7*, 75–86.
22. Gilbert, E.N. Capacity of a Burst-Noise Channel. *Bell Syst. Tech. J.* **1960**, *39*, 1253–1265.
23. Song, H.; Chen, S.C.; Yam, Y. Sliding Mode Control for Discrete-Time Systems with Markovian Packet Dropouts. *IEEE Trans. Cybern.* **2017**, *47*, 3669–3679.
24. Shen, Y.; Wang, Z.; Shen, B.; et al. Nonfragile H_∞ filtering for discrete multirate time-delayed systems over sensor networks characterized by Gilbert-Elliott models. *Int. J. Robust Nonlinear Control* **2020**, *30*, 3194–3214.
25. Brockett, R.W.; Liberzon, D. Quantized Feedback Stabilization of Linear Systems. *IEEE Trans. Autom. Control* **2000**, *45*, 1279–1289.
26. Kang, X.; Ishii, H. Coarsest quantization for networked control of uncertain linear systems. *Automatica* **2015**, *51*, 1–8.
27. Yan, Y.; Yu, S.; Yu, X. Quantized super-twisting algorithm based sliding mode control. *Automatica* **2019**, *105*, 43–48.
28. Li, J.; Niu, Y.; Ho, D.W.C. Limited Coding-Length-Based Sliding-Mode Control with Adaptive Quantizer's Parameter. *IEEE Trans. Autom. Control* **2022**, *67*, 6248–6255.
29. Zhou, S.; Song, J.; Lam, H.K.; et al. Coding-Decoding-Based Sliding Mode Control for Markovian Jump Systems under Constrained Bit Rate: An Adaptive Quantizer Approach. *IEEE Trans. Control Netw. Syst.* **2024**, *11*, 255–269.

30. Li, J.; Niu, Y.; Ho, D.W.C. Dynamic Coding-Based Control Scheme under Lossy Digital Network: An Optimized Time-Varying Packet Length Approach. *IEEE Trans. Cybern.* **2024**, *54*, 2955–2965.
31. Zhou, W.; Wang, Y.; Liang, Y. Sliding mode control for networked control systems: A brief survey. *ISA Trans.* **2022**, *124*, 249–259.
32. Liu, X.; Ling, Z.; Zhang, Y. Torus-Event-Based Sliding Mode Control for Networked Interval Type-2 Fuzzy Systems under Deception Attacks. *Int. J. Netw. Dyn. Intell.* **2025**, *4*, 100003.
33. Zhang, M.; Ding, D.; Shen, B.; et al. Integral Sliding Mode Control for Automated Vehicles under Coding-Decoding Mechanisms with Constrained Bit Rate. *IEEE Internet Things J.* **2025**, *12*, 16214–16226.
34. Zhang, H.; Yang, S.; Song, J.; et al. Sliding Mode Control for Persistent Dwell-Time Switched System under Multi-Node Round-Robin Protocol and Replay Attacks. *Int. J. Robust Nonlinear Control* **2026**, *36*, 4760–4774.
35. Xu, J.; Niu, Y. Sliding mode consensus control for multi-agent systems under multi-node round-robin protocol. *Franklin Open* **2023**, *5*, 100052.
36. Zhang, P.; Cao, Z.; Peng, C.; et al. Dynamic-Coding-Based Sliding Mode Control under Gilbert-Elliott Networks with FlexRay Protocol: The High-Rate Case. *IEEE Internet Things J.* **2026**, *13*, 12051–12063.
37. Cao, Z.; Niu, Y.; Peng, C. Finite-Time Stabilization of Uncertain Markovian Jump Systems: An Adaptive Gain-Scheduling Control Method. *IEEE Trans. Autom. Control* **2024**, *69*, 3531–3543.
38. Lou, H.; Jiang, B.; Kao, Y.; et al. A GA-based dynamic event-triggered adaptive sliding mode control of networked Markov jump systems. *Nonlinear Dyn.* **2025**, *113*, 18453–18468.
39. Zhang, L.; Jiang, Y.; Chen, G.; et al. Heading control of variable configuration unmanned ground vehicle using PID-type sliding mode control and steering control based on particle swarm optimization. *Nonlinear Dyn.* **2023**, *111*, 3359–3376.
40. Vijay, D.; Jayashree, R. Sliding Mode Controller Based on Genetic Algorithm and Simulated Annealing for Assured Crew Reentry Vehicle. *J. Aerosp. Eng.* **2023**, *36*, 04023039.
41. Ke, H.; Yang, Y.; Xu, Y.; et al. Simulated Annealing-Driven Event-Triggered Neural Sliding Mode Control for Networked Nonlinear Markov Jump Systems. *Electronics* **2026**, *15*, 1220.